ACS APPLIED MATERIALS & INTERFACES

Research Article

www.acsami.org

Influence of the Molecular Weight and Size Dispersion of the Electroluminescent Polymer on the Performance of Air-Stable Hybrid Light-Emitting Diodes

Eugenia Martinez-Ferrero,*[,†] Souren Grigorian,[‡] James W. Ryan,[§,†] Werther Cambarau,[§] and Emilio Palomares[§,∥]

[†]Fundació CETEMMSA, Avenida Ernest Lluch 36, E-08302 Mataró, Spain

[‡]Institute of Physics, University of Siegen, Walter-Flex-Strasse 3, D-57068 Siegen, Germany

[§]Chemical Research Institute of Catalonia (ICIQ), Avenida Països Catalans 16, E-43007 Tarragona, Spain

[∥]Institució Catalana de Recerca i Estudis Avançats (ICREA), Barcelona, Spain

Supporting Information

ABSTRACT: The influence of the chain length and the molecular weight distribution of the electroluminescent polymer on the carrier transport properties and morphology of air stable hybrid light-emitting diodes is reported. It is found that variations between diverse as-received commercial batches play a major role in the performance of the devices, whose maximum luminance can differ up to 2 orders of magnitude. Through complementary optoelectronic, structural, and morphological characterization techniques, we provide insights into the relationship between charge dynamics and the structure of polymeric electroluminescent materials. The carrier dynamics are found to be dominated by both the polymeric chain length and the hole transport, which in turn is dependent on the concentration of trap states. Furthermore, the chain length is seen to affect the morphology of the active layer.

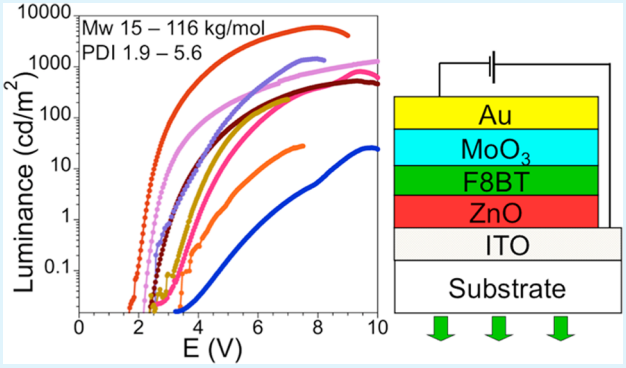

KEYWORDS: *electroluminescent polymers, hybrid light-emitting diodes, F8BT, molecular weight, polidispersity index, charge carrier mobility*

INTRODUCTION

The performance of optoelectronic devices relies heavily on the properties of the semiconducting polymers that make up the active layer. The packing of the molecular chains affects the charge transport in such a manner that polaron or exciton separation, charge transport, and recombination depend on the resulting morphology.[1−3] This has been reported in significant detail for many organic electronic devices, in particular organic solar cells and organic transistors,[4] where it has been demonstrated that the behavior of the polymer depends on its molecular weight, which can be difficult to control and can lead to large differences in device performance.[5] Furthermore, the chain length and its size distribution are also key factors that determine the packing of the polymer chains and their orientation toward the electrodes.[6] Indeed, the distance between the aromatic groups of adjacent chains also varies with the polymeric Mw resulting in different charge mobilities.[7−9] On the other hand, the polidispersity index (PDI) is ubiquitous, particularly in commercial grade samples, adding variability to the reproduction of the devices.

In this work, we explore the impact of the variations of the molecular weight and the PDI of commercial electroluminescent polymers. Despite numerous investigations of polymeric properties on the performance of organic field effect transistors and solar cell applications,[10−13] this topic has not been explored with the same intensity in the field of organic light emitting diodes (OLEDs).[14−16] Therefore, we have chosen these types of devices due to their potential as light sources and the major influence that the electroluminescent layer has on the properties of the device. However, despite their impressive efficiencies, one significant drawback of OLEDs is the use of low work function electrodes and organic transport layers that are sensitive to moisture and oxygen and require costly protective layers.[17] Therefore, it is desirable to replace the organic materials by stable transition metal oxides as charge transport layers. In this way, the robustness, transparency and electronic properties of the inorganic materials are then

Received: August 4, 2014
Accepted: December 18, 2014
Published: December 18, 2014

DOI: 10.1021/am505197b
ACS Appl. Mater. Interfaces 2015, 7, 1078−1086

Scheme 1. (a) Description of the HyLED Multilayered Structure, (b) the Chemical Structure of the F8BT Polymer, and (c) the Energy Band Diagram of the Device

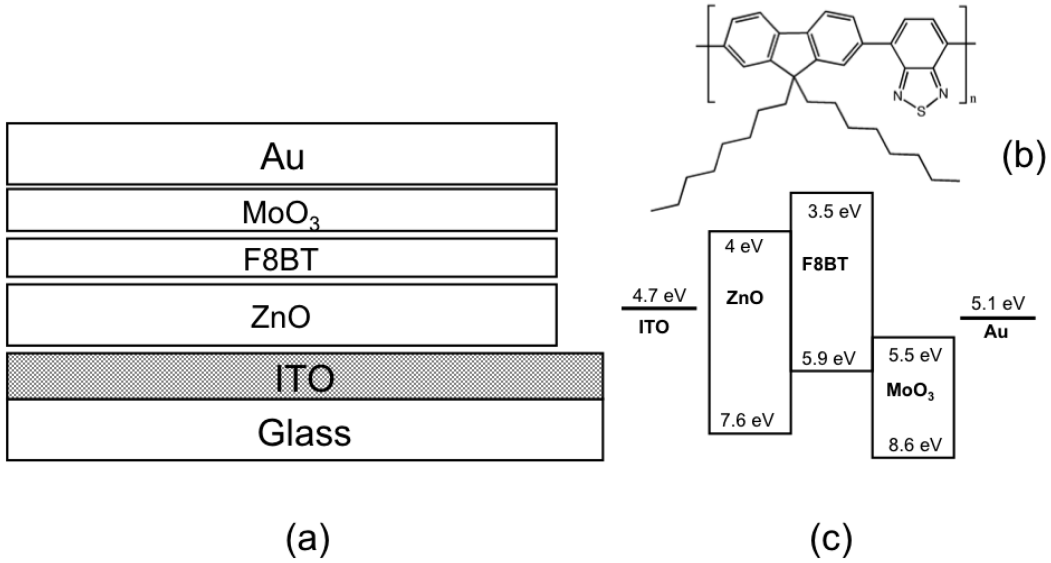

combined with the possibilities offered by the organic lumophores giving rise to hybrid light-emitting diodes (see Scheme 1). These devices, which have shown similar performances to those of the best published polymeric OLEDS,[18] are formed by sandwiching organic electroluminescent polymers between an electron transport layer (ETL) such as ZnO, TiO_2, or ZrO_2 and a MoO_3 hole transport layer (HTL) topped with an inert high work function gold anode.[19−21] In addition, the low cost and the facile preparation of the metal oxides permit the reduction of production costs and the fabrication of devices in air by solution methods. F8BT (*poly-9,9′-dioctylfluorene-alt-benzothiadiazole,* Scheme 1b) has been used as an electroluminescent polymer because it is widely used in organic electronics and its LUMO and HOMO levels match well with the conduction bands of the charge transport layers (Scheme 1c).

To focus exclusively on the variability of the semiconducting polymer, we have acquired different commercial batches of F8BT and tested them on devices with identical configurations. Depending on the batch, the maximum luminance achieved by the diodes can differ by up to 2 orders of magnitude and significant differences in the current−voltage characteristics are observed. To determine the key properties controlling the device performance, we have carried out a detailed study on the morphology, surface, and optical properties of the active layer. In addition, we have also probed the charge carrier dynamics of the devices under working conditions to obtain more detailed information on the effect of polymer structure on device performance.

EXPERIMENTAL SECTION

F8BT samples were acquired from different suppliers and their molecular weights measured by gel permeation chromatography against polystyrene standards (Table 1). The reported purities are 99.99% and metal contents, when indicated by the provider, below 84 ppm. Zinc acetate dihydrate, methanol, xylene and MoO_3 were purchased from Sigma-Aldrich and used as received.

Device Preparation and Characterization. The ZnO layers were prepared by spray pyrolysis deposition from a precursor solution of zinc acetate dihydrate in methanol (80 g/L) onto prepatterned ITO glass substrates (10 Ω/sq, obtained from Psiotec Ltd.) at 450 °C

Table 1. Description of the F8BT Batches Employed in This Work[a]

sample	M_n (g/mol)	M_w (g/mol)	PDI	supplier
F15k	5897	15686	2.7	Sigma-Aldrich
F23k	4107	23000	5.6	American Dye Source
F27k	12273	27000	2.2	1-Material
F35k	14583	35000	2.4	American Dye Source
F43k	17133	43517	2.5	Sigma-Aldrich
F60k	31579	60000	1.9	QCR Solutions
F73k	22812	73000	3.2	American Dye Source
F116k	34118	116000	3.4	American Dye Source

[a]PDI stands for the polidispersity index.

followed by annealing at 450 °C for 30 min. The electroluminescent F8BT layer was spin coated from a xylene solution and annealed at 155 °C for 30 min in a nitrogen rich atmosphere. The solution concentration was adjusted to get film thicknesses of 100 nm. Finally, the samples were transferred to a thermal evaporation chamber where the MoO_3 (15 nm) and Au (100 nm, Kurt Lesker) layers were deposited through a shadow mask under high vacuum (1×10^{-7} mbar), which defined an active area of 0.25 cm^2. The as-prepared devices were transferred out of the glovebox and measured in air without any form of encapsulation. The devices were characterized with a Thornlabs silicon photodiode combined with a Keithley 2400 source controlled by in-house software.

Hole-only devices were prepared and characterized following the same procedure than the bipolar diodes. The ZnO layer is substituted by 50 nm of PEDOT:PSS, which is deposited by spin coating and annealed under nitrogen at 120 °C for 30 min. The subsequent layers are deposited as described above.

Film Characterization. Thicknesses were measured by an Ambios Technology XP-1 profilometer and confirmed by X-ray reflectometry. Atomic Force Microscopy measurements were done in tapping mode on a Molecular Imaging model Pico SPM II while images were analyzed using WSxM software.[22] Grazing incident X-ray diffraction (GIXD) studies were performed using a high-resolution diffractometer Seifert XRD 3003 operating at 8 keV and equipped with a point detector. Out-of-plane GIXD profiles were measured at the fixed incident angle $\alpha = 0.17°$ being higher than the critical angle of the polymer film and lower than the critical angle of the substrate. The surface free energy was estimated by the Owens-Wendt-Rabel-Kaelble (OWRK) method from the contact angle measurements done on the

DOI: 10.1021/am505197b
ACS Appl. Mater. Interfaces 2015, 7, 1078−1086

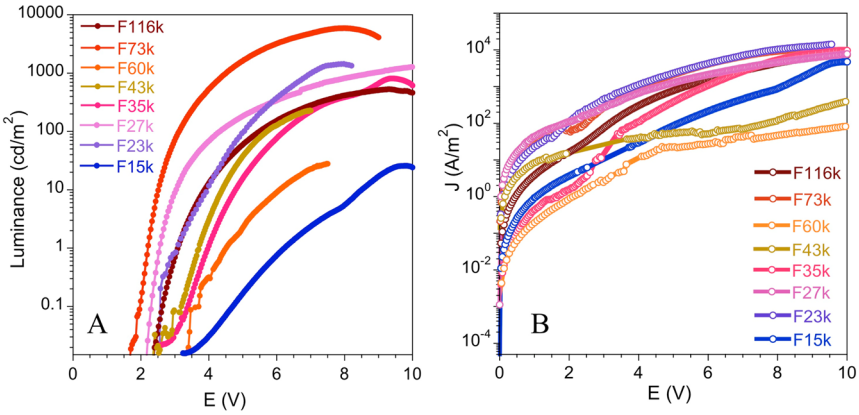

Figure 1. (a) Luminance and (b) current density vs applied bias for the ITO/ZnO/F8BT/MoO_3/Au devices prepared with F8BT of different M_w and PDI.

polymer films by means of a Krüss DSA100. Differential scanning calorimetry (DSC) and thermogravimetric analysis (TGA) were performed using a Mettler-Toledo TGA-DSC 1 under nitrogen. DSC experiments were carried out in two consecutive heating cycles from 30 to 300 and cooling back to 30 °C at a rate of 10 °C/min while TGA consisted in a single measurement from 30 to 500 °C at a rate of 20 °C/min. UV−visible absorption was measured in a PerkinElmer Lambda 950, whereas fluorescence measurements were recorded using an Aminco-Bowman Series 2 luminescence spectrometer. Time correlated single photon counting (TCSPC) experiments were carried out after recording 1000 counts per second (CPS) with a Lifespec picosecond fluorescence lifetime spectrophotometer from Edinburgh Instruments equipped with lasers as excitation sources. The instrument response was always shorter than 440 ps measured at full width half-maximum (fwhm). For transient electroluminescence measurements (TEL), the devices were electrically excited by a fast pulse generator Thurlby Thandar Instruments TGP110, which permitted accurate control of rise and decay times. Single square-wave voltage pulses between 4 and 7 V were applied during 100 μs. The electroluminescence response was detected using a PM Hamamatsu H6780−01 photomultiplier tube detector connected to an amplifier from Hamamatsu C9693. A Teknotronix TDS 2022 oscilloscope was used to record the voltage, time, and electroluminescence.

All the measurements were carried out at ambient conditions without using encapsulating layers.

RESULTS

The commercial samples employed in this study are summarized in Table 1. The hybrid light-emitting diodes (HyLEDs) were structured as ITO/ZnO/F8BT/MoO_3/Au and all the layers were deposited under the same conditions to permit a fair comparison of the behavior of the different polymers.

The diodes were characterized by measuring the evolution of light emission with applied bias (Figure 1). The devices present turn on voltages lower than 3 V and reach the maximum luminance below 10 V (see Table 2 and Table S1 in the Supporting Information). The best luminance values are achieved in devices containing the F73k sample, whereas poorer behaviors of up to 2 orders of magnitude lower are observed when F15k and F60k are employed. It is interesting to note that the turn-on voltages for the samples F15k, F60k, and F73k deviate from the mean estimated value of the other samples. This is rather surprising, because turn on voltages are related to the electron injection barrier, which is defined as the difference between the ITO workfunction and the metal oxide conduction band edge.[18]

Table 2. Optoelectronic Data of the Devices Obtained from the *L*−*V* Curve, the Fitting of the JV Curve, and TEL Measurements

sample	V_{on} (V)[a]	L_{max} (cd/m^2)[b]	μ_0 (cm^2/(V s))[c]	β (cm$^{1/2}$/V$^{1/2}$)[c]	V_{trap} (V)[d]
F15k	2.8	26	1.1×10^{-6}	4.1×10^{-3}	2.9
F23k	2.3	1440	4.3×10^{-5}	1.3×10^{-4}	2.7
F27k	2.1	1340	1.0×10^{-5}	1.0×10^{-4}	2.3
F35k	2.4	890	1.8×10^{-5}	1.2×10^{-3}	4.1
F43k	2.3	224	1.9×10^{-7}	3.9×10^{-3}	4.9
F60k	2.7	28	5.9×10^{-7}	3.9×10^{-4}	
F73k	1.8	6400	2.8×10^{-5}	9.0×10^{-4}	3.2
F116k	2.3	530	9.7×10^{-5}	7.3×10^{-4}	2.5

[a]The turn-on voltage is defined as the applied bias when the luminance reaches 0.01 cd/m^2. [b]Maximum luminance. [c]Data obtained from fitting the JV curves. [d]Data obtained from TEL measurements.

Figure 1b shows the evolution of the density current vs applied bias (Figure 1b) from a linear dependence that turns exponential at voltages closer to the built-in voltage (V_{bi}), pointing to the change from a diffusion dominated current into a space charge limited regime.[23] This fact arises from the energy band alignment of the different components of the device, described in Scheme 1c. The MoO_3 of the HTL forms an ohmic contact with the electroluminescent polymer allowing the injected holes to drift from the electrode to the organic−inorganic interface where they accumulate leading to a built in field, due to the energy mismatch between the valence band (VB) of the ETL and the HOMO of the polymer. The field assists the injected electrons on the other electrode to overpass the electron injection barrier between the conduction band (CB) of the ETL and the LUMO of the F8BT.[18] The charge transport at voltages higher than V_{bi} is thus bulk limited and is best described as pseudohole only space charge limited current, since the predominant carriers are holes.[24−26] The *J*−*V* curve can be modeled using the Mott−Gurney equation combined with field dependent mobility (eq 1)

$$J_{sclc} = \frac{9}{8}\varepsilon\mu_0\frac{V^2}{L^3}\exp\left[\beta\sqrt{\frac{V}{L}}\right] \quad (1)$$

where ε is the $\varepsilon_0\varepsilon_r$ permittivity of the F8BT polymer, μ_o is the hole zero field mobility, V is the effective applied bias (the applied bias corrected by the built-in potential), L is the thickness of the active layer and β is the field-effect mobility

DOI: 10.1021/am505197b
ACS Appl. Mater. Interfaces 2015, 7, 1078−1086

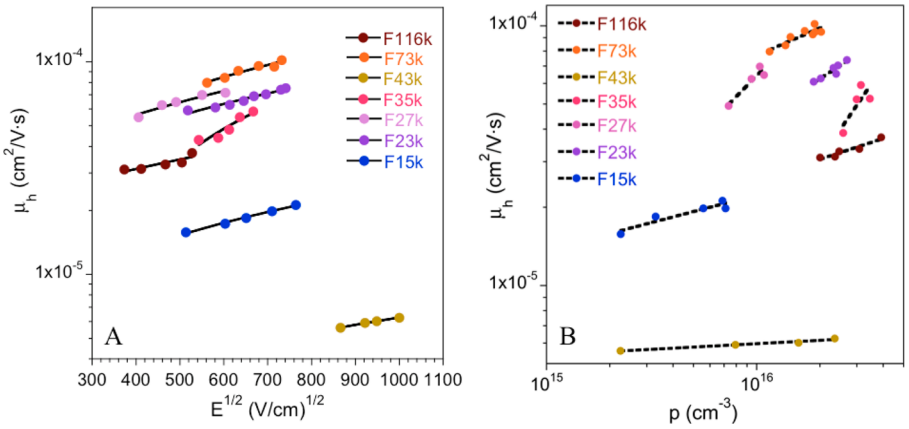

Figure 2. (a) Hole mobility as a function of the square root of the electric field and (b) variation of the hole mobility with the free hole density. Solid lines indicate linear fitting, dashed lines indicate power law fitting.

coefficient (also known as Poole-Frenkel factor). The parameters obtained from the fitting of the $J-V$ curves, listed in Table 2 and shown in the Supporting Information, indicate that the room temperature hole mobility μ_o amounts to ~1 × 10^{-5} $cm^2/(V\ s)$ for all the samples except for F15k, F43k, and F60k. The β coefficient, which depends upon trap depths, is estimated to be 1 × 10^{-4} $cm^{1/2}/V^{1/2}$, except for F15k, F35k, and F43k, which is 1 order of magnitude lower, suggesting an increased influence of traps in the charge carrier mobility. Comparison with parameters obtained from hole-only devices made of ITO/PEDOT:PSS/F8BT/MoO_3/Au when the hole injection takes place from the MoO_3 (see Table S2 and Figure S2 in the Supporting Information) indicate that the difference is less than one-fold and probably arises from the beneficial influence of the ZnO layer.

Independent measurements of the hole mobility under working conditions are obtained by transient electroluminescence (TEL) in which the time dependence of the rise of electroluminescence is recorded after application of square voltage pulses of different amplitude. The delay time (t_d) between the voltage start and the onset of light emission is a direct measurement of the transit time of the faster charge carriers (holes, vide supra) toward the recombination zone. Therefore, TEL curves can be well described by the equations used for hole-only single layer OLEDs, in which holes drift faster toward the interface dominating the early stage of the rising of electroluminescence.[27]

Once the holes reach the steady state, which occurs at times close to t_d, further rise of electroluminescence is then due to electron flow in the bulk. Even at this stage, hole density exceeds the electron concentration and is not affected by charge recombination. Consequently, we can estimate the hole mobility from the electroluminescence output using the equation of the drift mobility in a electric field (eq 2)

$$\mu_h = \frac{L^2}{Vt_d} \tag{2}$$

where L accounts for the thickness of the active layer, V is the effective applied bias ($V-V_{bi}$) and t_d is the time delay. Figure 2a illustrates the linear dependence of the as-estimated μ_h with the electric field, except for F60k that could not be measured due to its low luminance. The variation between samples corroborates the previous observations of Figure 1b in the sense that charge dynamics are influenced by the molecular weight and PDI.

Further information can be obtained following the development made by Rihani et al., who estimated the free hole density (p_e) considering the Langevin charge recombination coefficient (R) and the recombination current, J_r.[27] Briefly, R can be estimated from the hole mobility through eq 3.

$$R = \frac{q\mu_h}{\varepsilon} \tag{3}$$

where q stands for the elementary charge, μ_h is the hole mobility and ε is the permittivity of F8BT. Furthermore, the recombination current is directly proportional to the light emission. Therefore, from the evolution of light emission with time we can estimate the time constant τ (eq 4), which is inversely proportional to the free hole density, p_e. Equation 5 demonstrates this relationship where EL refers to the electroluminescent signal at a given time t and a is the value of the intersection at time 0

$$\ln\left[\frac{\mathrm{EL}(t\to\infty) - \mathrm{EL}(t)}{\mathrm{EL}(t\to\infty)}\right] = a - \frac{t}{\tau} \tag{4}$$

$$p_e = \frac{\tau^{-1}}{R} \tag{5}$$

The as-calculated free hole densities (eq 5) depend linearly with the applied bias so extrapolation to lower bias indicates that p_e vanishes at certain voltages pointing to the presence of traps in the bulk (V_{trap}, see Table 2). Therefore, the low charge carrier density at lower applied bias is due to the fact that the empty traps are becoming filled. As the applied voltage increases, the number of empty traps decreases and the number of free holes increases, resulting in enhanced current densities. A close inspection reveals that V_{trap} is similar to $V_{turn\text{-}on}$ suggesting that, at lower bias, the dominant mechanism is nonradiative trap assisted recombination in agreement with previous observations.[23] The exception is found for the samples F35k, F43K, and to a lesser extent F73k, which show higher V_{trap} than the rest. Again, comparison of this data with that obtained from the $J-V$ curve reveals that these samples possess high β values, confirming the increased influence of the traps on the mobility values.

On the other hand, the variation in μ_h with charge carrier density follows a power law trend (Figure 2b), in agreement with the conduct observed for other polymers at charge carrier densities higher than 1 × 10^{16} cm^{-3}.[28] The dependence of the

DOI: 10.1021/am505197b
ACS Appl. Mater. Interfaces 2015, 7, 1078−1086

field-effect mobility on charge carrier density has been related to the width of the exponential density of states; therefore, the stronger dependence of the mobility on the charge carrier density in samples F35k and F27k are indicative of larger energetic disorder.[28] Moreover, the analysis of the charge dynamics suggests a major influence of traps on the performance of the diodes. The device F43k display lower charge carrier mobility reflected in reduced free hole density and current density together with high values of β and V_{trap}. Moreover, the devices with lower current densities (F15k, F43k, and F60k) lead to higher luminance turn-on voltages regardless of the electron injection barrier. In addition, these samples give poorer luminance.

However, the charge mobility does not correlate with the variations in the M_w or the PDI. Consequently and in order to gain further information, we have undertaken optical and morphological studies on polymer films. The absorption spectra, shown in Figure 3a, present the typical pattern for F8BT with the main peak centered at 465 nm. The fact that the peaks are not significantly shifted or broadened suggests that the optical band gap does not change regardless of the Mw and the PDI. Photoemission measurements after excitation at 450 nm, Figure 3b, show a main signal centered at 536 nm except for F116k whose emission maximum is red-shifted to 541 nm. The intensity of the peaks varies according to their respective PDI suggesting that higher size dispersion is more beneficial to efficient light emission than higher Mw.

Time-correlated single photon counting (TCSPC) records the decay signals as a function of time after excitation at 405 nm. The experimental points are fitted with eq 6

$$I(t) = I_0 \exp[-(t/\tau)] \quad (6)$$

where $I(t)$ represents the time (t) dependent decay of the fluorescence intensity, I_o stands for the initial intensity values and τ is the lifetime value obtained from the decay, indicating the average time that the polymer remains in the excited state. Figure 3c shows the decays for all the samples. F15k, F43k, and F60k fall within the response of the instrument (IRF) and thus, the decays are shorter than 0.44 ns. The rest of the samples show monoexponential decays that can be fitted to eq 6, resulting in lifetime values that are shown in Table 3.

Additionally, we have measured the lifetime of the devices under ambient conditions. Measurements were done every 24 h on devices without encapsulation that were stored in air. The results, which have reached values of 600 h, do not show significant differences between the most efficient polymers.

To gain further insight into the relationship between the molecular weight distribution and the morphology, we have proceeded with differential scanning calorimetry (DSC). Figure 4 shows the second heating scan, where the first feature above 100 °C is an endothermic transition followed by an exothermic peak around 150 °C. The combinations of the first cooling scan with the second heating scan indicates that it is due to the transition of the polymer from the glassy to the rubbery state that takes place alongside a crystallization step.[29] The glass transition temperature (T_g) has been therefore estimated at the onset of the first change of the heat capacity defined by the point of intersection between the baseline before the thermal effect and the tangent of the curve (Table 4). A second exothermic transition located around 185 °C is assigned to further crystallization. Finally, there is the onset of a third transition at temperatures around 200 °C. The endothermic nature of the smooth transition points to the occurrence of the melting process to liquid crystalline phase.

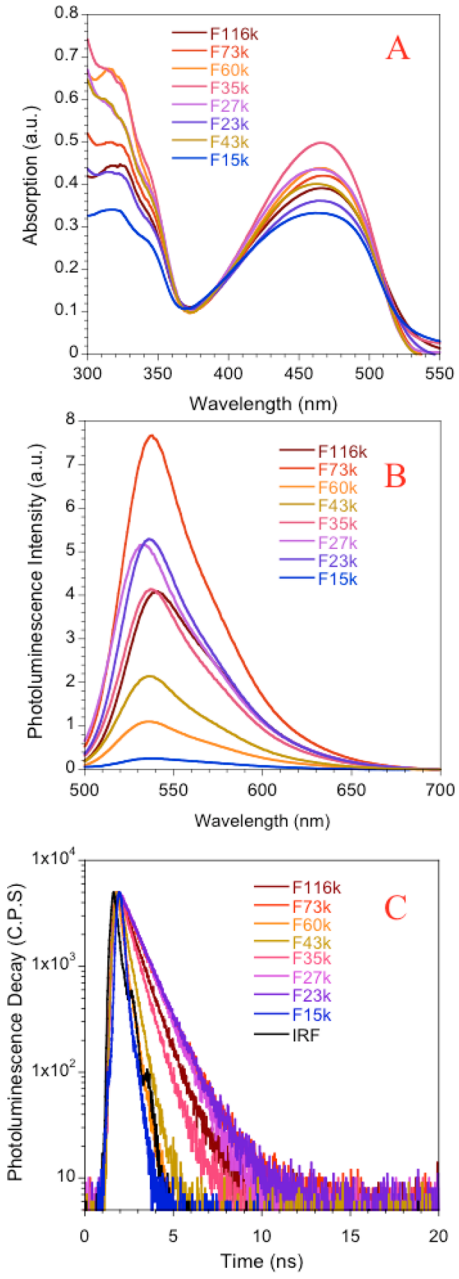

Figure 3. Optical characterization of F8BT thin films (a) UV−vis absorption, (b) photoluminescence, (c) TCSPC decays (IRF: instrument response function).

Table 3. Photophysical Parameters of the Polymeric Films

sample	λ_{max} Abs (nm)	λ_{max} PL (nm)	τ (ns)
F15k	464	537	<0.44
F23k	464	536	1.55
F27k	462	532	1.45
F35k	465	537	1.30
F43k	462	536	<0.44
F60k	465	536	<0.44
F73k	467	538	1.57
F116k	466	541	1.32

DOI: 10.1021/am505197b
ACS Appl. Mater. Interfaces 2015, 7, 1078−1086

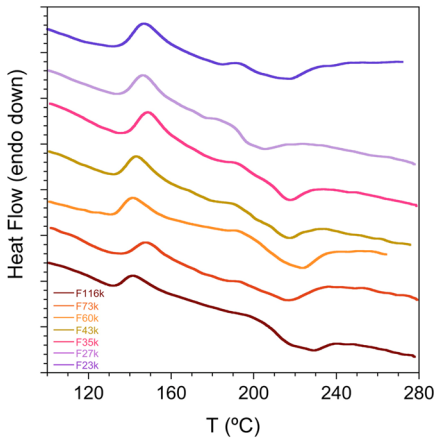

Figure 4. DSC data of the second heating scan for all the polymers.

Table 4. Temperature of the Glass Transition (T_g), Wettability Properties Described by the Surface Energy (γ_e) and the Dispersive (σ^D) and Polar Components (σ^P), the Crystalline Size (S) Calculated by GIXS, and Surface Average Roughness (Rav) of the F8BT Films

film	T_g (°C)	γ_e (mJ/m^2)	σ^D (mJ/m^2)	σ^P (mJ/m^2)	S (nm)	R_{AV} (nm)
F15k		27.5	27.2	0.3		2.2
F23k	104	29.9	29.7	0.2	15.2	2.3
F27k	107	28.3	27.9	0.4	16.9	3.1
F35k	109	28.1	27.8	0.3	14.2	3.0
F43k	104	27.9	27.7	0.2	30.6	2.8
F60k	101	29.7	29.5	0.2	9.7	1.8
F73k	109	29.7	29.6	0.1	11.2	2.6
F116k	112	30.4	30.3	0.1	13.3	3.8

Structural analysis to probe ordering was performed by GIXD measurements at the incident angle of $\alpha_i = 0.17°$. This incident angle is above the critical angle of the polymer ($\alpha_c = 0.15°$) and below that of the glass substrate ($\alpha_c = 0.21°$) to permit the penetration of the X-beam through the depth of the whole film. Figure 5 shows the scattering profiles, which present a peak at small angles suggesting the presence of similar structural organization of crystalline domains regardless of the Mw or PDI of the samples (see the Supporting Information, Figure S3). The peaks at higher angles could not be resolved

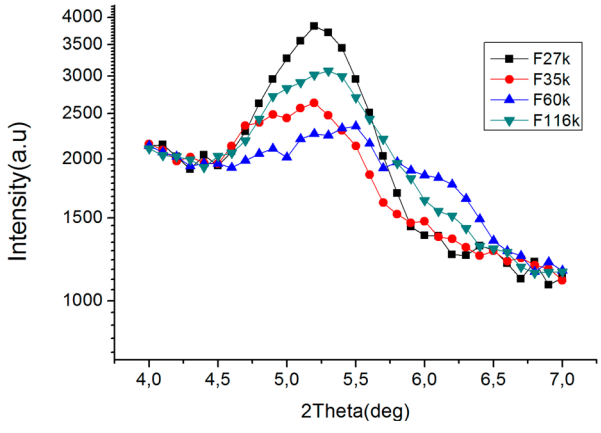

Figure 5. Out-of-plane GIXD in the vicinity of the (100) peak of F8BT films.

despite long counting time (200s) because of the weak signals arising from the low thickness of the samples. Therefore, X-ray studies were focused on the most intense scattering peaks centered at a 2θ position of ~5.2° (see Figure 5). According to the literature, polyfluorenes usually form lamellas that stack parallel to the substrate in a configuration described as the β-phase and defined by the $\pi-\pi$ stacking, the size of the F8-BT repeating unit and the interchain spacing.[30,9] We have focused on the peak corresponding to the interchain spacing that lies between 1.66 to 1.69 nm, depending on the sample, which agrees with the 1.6 nm reported in the literature.[30] Moreover, since the estimated length of the alkyl side chains is 8.75 Å we can deduce that the observed interchain distance corresponds to two polyfluorene backbones separated by alkyl chains. Similar edge-on orientation with the strongest (100) peak associated with side-chain distances along the out-of-plane direction has been reported for a large family of thiophenes.[31,32] All samples here show these characteristic features but for three exceptions, the F60k, F73k, and F43k samples. The first, F60k, shows a rather broad distribution shifted to higher 2θ angles with two peak positions suggesting the existence of two polymorphs where the chains are separated by 1.6 or 1.4 nm. In addition, it confirms the higher amount of disordered domains for the F60k in comparison to all other samples in the series that provide narrower peaks. Interestingly, F73k and F43k samples in turn show just one peak (very intense for F73k) located at even higher 2θ angles (see the Supporting Information) that correspond to interchain distances of about 1.2 nm. The size of the crystallites is obtained from the width of the peak in combination with the Scherrer equation (Table 4). The as-calculated size of the domains ranges from 10 to 17 nm with marginal changes of crystalline domains as a function of the molecular weight, except for F43k, which measures 30 nm.

Further information has been obtained by AFM studies (Figure 6). It is interesting to point out the low roughness of the samples ranging between 1.8 and 3.4 nm (see Table 4). The films are all formed by domains of aggregated crystallites that agree with literature reports about the polycrystalline nature of films forming well-ordered domains when annealed above T_g.[29,33] However, there are clear differences in the local morphology. The pattern in F43k is formed by long chains

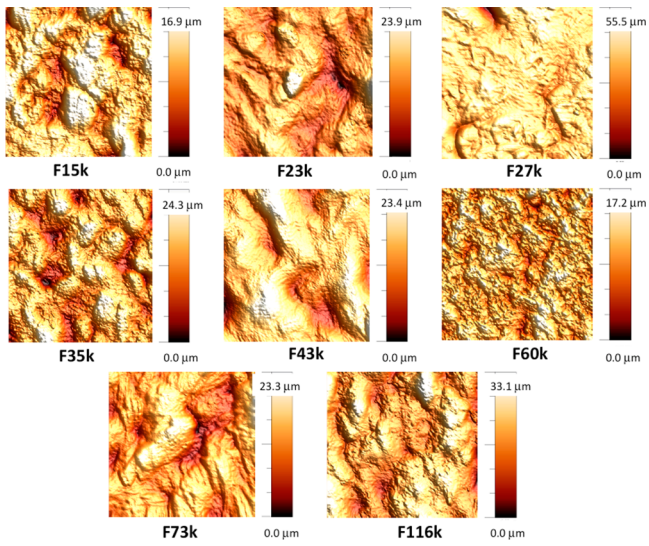

Figure 6. AFM topography images (2 μm × 2 μm) of the F8BT films.

DOI: 10.1021/am505197b
ACS Appl. Mater. Interfaces 2015, 7, 1078−1086

while the aggregates are much closer in F15K and F60k. Samples F23k, F35k, F73k, and F116k are arranged in a similar fashion than F43k, whereas the F27k film is rather smooth but contains aggregates of 200 × 140 nm. It is worth noting that F60k, which has the lowest PDI among the samples, forms small aggregates, whereas larger domains are observed in samples with PDI values above 2.5.

The formation of molecular aggregates is known to be strongly affected by the surface energy of the molecules.[34] Consequently, we have estimated the surface free energy of the different samples through the measurement of the contact angle of water, ethylene glycol and dimethyl sulfoxide on F8BT films. These values are applied in eq 7 to calculate the dispersive and polar interactions between F8BT and the liquids.

$$\frac{\sigma_L(1+\cos\theta)}{2\sqrt{\sigma_L^D}} = \sqrt{\sigma_S^P}\frac{\sqrt{\sigma_L^P}}{\sqrt{\sigma_L^D}} + \sqrt{\sigma_S^D} \quad (7)$$

where θ is the contact angle and σ is the surface free energy of the F8BT (S) or the liquid (L). The total surface energy is calculated from the sum of the dispersive and the polar components and the results are summarized in Table 4. The results indicate that surface free energy (SFE) increases with the Mw especially due to the decrease of the polar component. These observations agree with those of Wu, who defined a linear variation between the surface energy and $Mn^{-2/3}$, so the variation of the M_w provides a reliable method to control the surface energy.[34,35] However, the increase in M_w alone cannot explain the differences found in the structural characterization. The SFE of the chain ends is usually lower than that of the chain; therefore the increment of SFE values with higher Mw is assigned to the decreased ratio of chain ends to the repeat unit. The heterogeneity caused by the chain ends in the surface energy can affect the grain boundaries, the size of the domains and the order of the molecular arrangement.[34] Moreover, it could be the cause of the irregular change in the mobility of semiconducting layers.[36] In addition, we also need to consider the value of the PDI of each sample because it affects the heterogeneity of the surface as well. For example, on one hand, F60k has the lowest PDI, 1.9, shows the lowest mobility and forms films containing a broad dispersion of crystallites with a mean size of 9 nm arranged in a closed pattern resulting in low surface roughness. On the other hand, F23k has the highest PDI, 5.6, the charge mobility and luminance values are among the highest of the samples and it forms large and homogeneous domains (15.2 nm) resulting in relatively rougher films. In fact, the SFE values are higher than expected for this Mw and the polar component is comparable to F43k. So we can deduce that the polymer samples with higher PDI (F23k, F35k, F43k, F73k, and F116k) produce films with bigger domains that form large patterns as seen in the AFM images. The SFE values correlate with the M_w, although some subtle deviations are observed that are mainly due to the influence of the PDI on the heterogeneity of the surface. Finally, and although the films present certain surface roughness, it is worthy noticing that the average values are lower than 4 nm, and as reported by Wang et al., in these cases, the influence of the topography can be considered negligible.[37] On the other hand, the measurements of the contact angle have been done using the advancing angle, which has been demonstrated to be relatively less sensitive to surface roughness.[38] Therefore, the influence of the surface roughness on the measurements of the contact angle, and therefore on the determination of the SFE, have not been taken into account.

DISCUSSION

We have prepared devices with commercial F8BT samples ranging from 15686 to 116000 g/mol that present a broad dispersion of sizes. The performance of the devices depends on the morphology of the active layer, which in turns depends on the polidispersity index and chain length of the polymer, as summarized in Table 5. We consider first the samples F43k and F60k. The estimated charge carrier mobilities and current densities are lower than the rest of the samples, and consequently, the devices offer poor results with low luminance values and high turn-on voltages. This trend is also observed in the optical properties where the emission rates and the lifetime of the photogenerated excitons are also lower. But despite the similar optoelectronic properties of these two devices, their morphologies differ and so do the reasons for their poor behavior. F60k is composed of two polymorphs that form small crystalline domains. The features of the polymorphism have been detected by GIXD and by the width of the endothermic peak at DSC measurements, which despite its lower PDI displays a broad feature. The increased number of domains implies the presence of more grain boundaries that act as traps, which hinder charge transport and photoemission. On the other hand, F43k possess shorter spacing between polymer chains that can induce the formation of well-ordered nanodomains. The presence of these crystalline domains has not been detected by optical measurements but the structural analysis reveals the closer interchain spacing that gives rise to homogeneous domains ranging up to 30 nm. The decrease of spacing between polymer chains causes a decrease of the charge

Table 5. Summary of the Experimental Results Observed in Each Sample

sample	M_w (g/mol)	PDI	experimental observations
F15k	15686	2.7	shortest polymer chain length and moderate PDI
			poor charge mobility and optical properties
			poor device performance
F23k	23000	5.6	broad dispersion of chain lengths
			large crystalline domains
			excellent device performance
F27k	27000	2.2	moderate polydispersity
			formation of large aggregates
			excellent device performance
F35k	35000	2.4	moderate polydispersity
			high values for V_{trap}
			good device performance
F43k	43517	2.5	short interchain distances generating large domains
			poor charge mobility and optical properties
			moderate device performance
F60k	60000	1.9	presence of polymorphs and impurities
			small domains originating grain boundaries
			poor mobility and optical properties
			poor device performance
F73k	73000	3.2	high molecular weight and polydispersity
			short interchain distances, strong orientation of the chains
			excellent device performance
F116k	116000	3.4	high molecular weight and polydispersity
			formation of optical nonemissive aggregates
			moderate device performance

DOI: 10.1021/am505197b
ACS Appl. Mater. Interfaces 2015, 7, 1078−1086

mobility. This effect is also seen for F60k, where one of the polymorphs shares similar structural characteristics with F43k. Interestingly, the sample F73k with shorter interlammelae distance due to interdigitation of the side chains provides relatively high field effect mobility and the highest luminance. Despite that in samples F43k and F60k such interdigitations cause a dramatic decrease of the optoelectronics characteristics, the sample F73k reveals the best performance. The origin of this enhancement can be related to the strong improvement of the orientation features confirmed by the highest intensity of the out-of-plane GIXD profile. Thermogravimetric analysis of F60k reveals an unusual loss of weight between 100 and 360 °C that have not seen in the rest of the samples (see the Supporting Information).

Samples F15K, F23k, F27k, F35k, F73k, and F116k display similar morphological features with homogeneous domains made of crystallites of similar sizes giving rise to moderate surface roughness. The performance of the devices improves with increasing length of the polymer chains, and therefore, F15k has low luminance values coincident with lower mobility values. This trend is usually assigned to the concentration of chain ends that can act as trapping centers. However, F116k does not produce the best device, as the trend would suggest. Reasons for the lower than expected performance can be deduced from the red shift of the photoluminescence peak and a moderate increase in the roughness of the film surface that suggests the formation of nonemissive aggregates. These aggregates could originate from partial chain entanglements that limit molecular motion and crystallization despite the annealing treatment.[29] Finally, it is worth mentioning F23k, which behaves better than expected for its M_w. A priori, the chain ends act as exciton dissociation sites so shorter polymer chains with more chain ends are expected to have lower emission efficiency, but this effect is mitigated by the broad dispersion of chain lengths in the sample that contribute to increase the photoluminescent efficiency. As has been reported before, polydispersity enhances the ability of polymers to self-organize during the annealing process at optimized temperatures. In fact, devices made of P3HT with low M_w and high polidispersity have been observed to be more efficient than devices with higher M_w due to the enhanced crystallinity of the polymer chains.[39] On the other hand, the presence of small fractions of high molecular weight polymers can drastically affect film formation in blends with polymers of lower M_w, their morphology and carrier dynamics.[40] Finally, if we are to conclude on any general trend from the experimental results, high PDI values favor good optical properties and the formation of large domains, which result in enhanced performance of the devices.

CONCLUSIONS

In conclusion, this study determines the influence of the molecular weight and polidispersity index of commercial F8BT in the performance of hybrid light-emitting diodes. Contrary to previous work on this topic made on purified polymers, the commercial batches have broad size dispersion that affects the performance of the devices. So, despite higher M_w favors charge mobility, the presence of long polymer chains does not always guarantee the formation of adequate morphologies that lead to efficient devices. Consequently, it is necessary to consider the molecular weight, the size distribution, and the purity of the batches because of their influence on the morphology and the final properties of the devices.

We believe that these conclusions will impact several important research fields where polymers are utilized such as organic solar cells, light-emitting diodes, and transistors promoting the industrial development of optoelectronic devices.

ASSOCIATED CONTENT

Supporting Information

Fittings of the $J-V$ curve of bipolar and hole-only devices, long-range out-of-plane GIXD data and thermogravimetric analysis of the polymers. This material is available free of charge via the Internet at http://pubs.acs.org.

AUTHOR INFORMATION

Corresponding Author

* Fax: +34 93 741 9228; Tel: +34 93 741 9100; E-mail: emartinez@cetemmsa.com.

Present Address

[†]Department of Chemistry, The University of Tokyo, 7−3−1 Hongo, Bunkyo-ku, Tokyo 113−0033 (Japan)

Author Contributions

The manuscript was written through contributions of all authors. All authors have given approval to the final version of the manuscript.

Notes

The authors declare no competing financial interest.

ACKNOWLEDGMENTS

E.M-F. thanks the Spanish MINECO for the Ramon y Cajal fellowship RYC-2010-06787 and funding through the project MAT2012-31570. C. Carenas' help for the acquisition of TEL data is acknowledged. S.G. is grateful to L. Grodd and C. Kwamen for assistance during X-ray measurements and to BMBF for financial support through the project Nr05K13PS4. Financial support from CETEMMSA is appreciated as well.

REFERENCES

(1) Ballantyne, A. M.; Chen, L.; Dane, J.; Hammant, T.; Braun, F. M.; Heeney, M.; Duffy, W.; McCulloch, I.; Bradley, D. D. C.; Nelson, J. The Effect of Poly(3-hexylthiophene) Molecular Weight on Charge Transport and the Performance of Polymer:Fullerene Solar Cells. *Adv. Funct. Mater.* **2008**, *18*, 2373−2380.

(2) Salleo, A.; Kline, R. J.; DeLongchamp, D. M.; Chabinyc, M. L. Microstructural Characterization and Charge Transport in Thin Films of Conjugated Polymers. *Adv. Mater.* **2010**, *22*, 3812−3838.

(3) Cornil, J.; Beljonne, D.; Calbert, J. P.; Brédas, J. L. Interchain Interactions in Organic π-Conjugated Materials: Impact on Electronic Structure, Optical Response, and Charge Transport. *Adv. Mater.* **2001**, *13*, 1053−1067.

(4) Chu, T.-Y.; Lu, J.; Beaupré, S.; Zhang, Y.; Pouliot, J.-R.; Zhou, J.; Najari, A.; Leclerc, M.; Tao, Y. Effects of the Molecular Weight and the Side-Chain Length on the Photovoltaic Performance of Dithienosilole/Thienopyrrolodione Copolymers. *Adv. Funct. Mater.* **2012**, *22*, 2345−2351.

(5) Kline, R. J.; McGehee, M. D.; Kadnikova, E. N.; Liu, J.; Fréchet, J. M. J.; Toney, M. F. Dependence of Regioregular Poly(3-hexylthiophene) Film Morphology and Field-Effect Mobility on Molecular Weight. *Macromolecules* **2005**, *38*, 3312−3319.

(6) Hiorns, R. C.; de Bettignies, R.; Leroy, J.; Bailly, S.; Firon, M.; Sentein, C.; Khoukh, A.; Preud'homme, H.; Dagron-Lartigau, C. High Molecular Weights, Polydispersities, and Annealing Temperatures in the Optimization of Bulk-Heterojunction Photovoltaic Cells Based on Poly(3-hexylthiophene) or Poly(3-butylthiophene). *Adv. Funct. Mater.* **2006**, *16*, 2263−2273.

DOI: 10.1021/am505197b
ACS Appl. Mater. Interfaces 2015, 7, 1078−1086

(7) Joshi, S.; Pingel, P.; Grigorian, S.; Panzner, T.; Pietsch, U.; Neher, D.; Forster, M.; Scherf, U. Bimodal Temperature Behavior of Structure and Mobility in High Molecular Weight P3HT Thin Films. *Macromolecules* **2009**, *42*, 4651−4660.
(8) Joshi, S.; Grigorian, S.; Pietsch, U.; Pingel, P.; Zen, A.; Neher, D.; Scherf, U. Thickness Dependence of the Crystalline Structure and Hole Mobility in Thin Films of Low Molecular Weight Poly(3-hexylthiophene). *Macromolecules* **2008**, *41*, 6800−6808.
(9) Donley, C. L.; Zaumseil, J.; Andreasen, J. W.; Nielsen, M. M.; Sirringhaus, H.; Friend, R. H.; Kim, J.-S. Effects of Packing Structure on the Optoelectronic and Charge Transport Properties in Poly(9,9-di-n-octylfluorene-alt-benzothiadiazole). *J. Am. Chem. Soc.* **2005**, *127*, 12890−12899.
(10) Tumbleston, J. R.; Collins, B. A.; Yang, L.; Stuart, A. C.; Gann, E.; Ma, W.; You, W.; Ade, H. The Influence of Molecular Orientation on Organic Bulk Heterojunction Solar Cells. *Nat. Photonics* **2014**, *8*, 385−391.
(11) Merari Masillamani, A.; Orgiu, E.; Samori, P. Effect of the Molecular Weight of the Polymer Gate Dielectric on the Performances of Solution-processed Ambipolar OTFTs. *Journal of Materials Chemistry C* **2013**, *1*, 7725−7730.
(12) Intemann, J. J.; Yao, K.; Yip, H.-L.; Xu, Y.-X.; Li, Y.-X.; Liang, P.-W.; Ding, F.-Z.; Li, X.; Jen, A. K. Y. Molecular Weight Effect on the Absorption, Charge Carrier Mobility, and Photovoltaic Performance of an Indacenodiselenophene-Based Ladder-Type Polymer. *Chem. Mater.* **2013**, *25*, 3188−3195.
(13) Fitzner, R.; Mena-Osteritz, E.; Mishra, A.; Schulz, G.; Reinold, E.; Weil, M.; Körner, C.; Ziehlke, H.; Elschner, C.; Leo, K.; Riede, M.; Pfeiffer, M.; Uhrich, C.; Bäuerle, P. Correlation of π-Conjugated Oligomer Structure with Film Morphology and Organic Solar Cell Performance. *J. Am. Chem. Soc.* **2012**, *134*, 11064−11067.
(14) Haldi, A.; Kimyonok, A.; Domercq, B.; Hayden, L. E.; Jones, S. C.; Marder, S. R.; Weck, M.; Kippelen, B. Optimization of Orange-Emitting Electrophosphorescent Copolymers for Organic Light-Emitting Diodes. *Adv. Funct. Mater.* **2008**, *18*, 3056−3062.
(15) Yim, K.-H.; Doherty, W. J.; Salaneck, W. R.; Murphy, C. E.; Friend, R. H.; Kim, J.-S. Phase-Separated Thin Film Structures for Efficient Polymer Blend Light-Emitting Diodes. *Nano Lett.* **2010**, *10*, 385−392.
(16) Weinfurtner, K.-H.; Fujikawa, H.; Tokito, S.; Taga, Y. Highly Efficient Pure Blue Electroluminescence from Polyfluorene: Influence of the Molecular Weight Distribution on the Aggregation Tendency. *Appl. Phys. Lett.* **2000**, *76*, 2502−2504.
(17) So, F.; Kondakov, D. Degradation Mechanisms in Small-Molecule and Polymer Organic Light-Emitting Diodes. *Adv. Mater.* **2010**, *22*, 3762−3777.
(18) Sessolo, M.; Bolink, H. J. Hybrid Organic−Inorganic Light-Emitting Diodes. *Adv. Mater.* **2011**, *23*, 1829−1845.
(19) Bolink, H. J.; Coronado, E.; Sessolo, M. White Hybrid Organic-Inorganic Light-Emitting Diode Using ZnO as the Air-Stable Cathode. *Chem. Mater.* **2009**, *21*, 439−441.
(20) Tokmoldin, N.; Griffiths, N.; Bradley, D. D. C.; Haque, S. A. A Hybrid Inorganic-Organic Semiconductor Light-Emitting Diode Using ZrO2 as an Electron-Injection Layer. *Adv. Mater.* **2009**, *21*, 3475−3478.
(21) Morii, K.; Kawase, T.; Inoue, S. High Efficiency and Stability in Air of the Encapsulation-free Hybrid Organic-inorganic Light-emitting Diode. *Appl. Phys. Lett.* **2008**, *92*, 213304/213301−213304/213303.
(22) Horcas, I.; Fernández, R.; Gómez-Rodríguez, J. M.; Colchero, J.; Gómez-Herrero, J.; Baro, A. M. WSXM: A Software for Scanning Probe Microscopy and a Tool for Nanotechnology. *Rev. Sci. Instrum.* **2007**, *78*, 013705.
(23) Wetzelaer, G. A. H.; Kuik, M.; Nicolai, H. T.; Blom, P. W. M. Trap-assisted and Langevin-type Recombination in Organic Light-emitting Diodes. *Phys. Rev. B* **2011**, *83*, 165204.
(24) Kabra, D.; Lu, L. P.; Song, M. H.; Snaith, H. J.; Friend, R. H. Efficient Single-Layer Polymer Light-Emitting Diodes. *Adv. Mater.* **2010**, *22*, 3194−3198.
(25) Lu, L. P.; Kabra, D.; Friend, R. H. Barium Hydroxide as an Interlayer Between Zinc Oxide and a Luminescent Conjugated Polymer for Light-Emitting Diodes. *Adv. Funct. Mater.* **2012**, *22*, 4165−4171.
(26) Lu, L.-P.; Kabra, D.; Johnson, K.; Friend, R. H. Charge-Carrier Balance and Color Purity in Polyfluorene Polymer Blends for Blue Light-Emitting Diodes. *Adv. Funct. Mater.* **2012**, *22*, 144−150.
(27) Rihani, A.; Hassine, L.; Fave, J. L.; Bouchriha, H. Study of the Transient EL Slow Rise in Single Layer OLEDs. *Org. Electron.* **2006**, *7*, 1−7.
(28) Tanase, C.; Meijer, E. J.; Blom, P. W. M.; de Leeuw, D. M. Unification of the Hole Transport in Polymeric Field-Effect Transistors and Light-Emitting Diodes. *Phys. Rev. Lett.* **2003**, *91*, 216601.
(29) Banach, M. J.; Friend, R. H.; Sirringhaus, H. Influence of the Molecular Weight on the Thermotropic Alignment of Thin Liquid Crystalline Polyfluorene Copolymer Films. *Macromolecules* **2003**, *36*, 2838−2844.
(30) Faria, G. C.; Plivelic, T. S.; Cossiello, R. F.; Souza, A. A.; Atvars, T. D. Z.; Torriani, I. L.; deAzevedo, E. R. A Multitechnique Study of Structure and Dynamics of Polyfluorene Cast Films and the Influence on Their Photoluminescence. *J. Phys. Chem. B* **2009**, *113*, 11403−11413.
(31) Hukic-Markosian, G.; Basel, T.; Singh, S.; Valy Vardeny, Z.; Li, S.; Laird, D. Study of Photoexcitations in Poly(3-hexylthiophene) for Photovoltaic Applications. *Appl. Phys. Lett.* **2012**, *100*, 213903.
(32) Bao, Z.; Lovinger, A. J. Soluble Regioregular Polythiophene Derivatives as Semiconducting Materials for Field-Effect Transistors. *Chem. Mater.* **1999**, *11*, 2607−2612.
(33) Watts, B.; Schuettfort, T.; McNeill, C. R. Mapping of Domain Orientation and Molecular Order in Polycrystalline Semiconducting Polymer Films with Soft X-Ray Microscopy. *Adv. Funct. Mater.* **2011**, *21*, 1122−1131.
(34) Sun, X.; Liu, Y.; Di, C.-A.; Wen, Y.; Guo, Y.; Zhang, L.; Zhao, Y.; Yu, G. Interfacial Heterogeneity of Surface Energy in Organic Field-Effect Transistors. *Adv. Mater.* **2011**, *23*, 1009−1014.
(35) Wu, S. *Polymer Interface and Adhesion*, 1st ed.; Taylor & Francis: New York, 1982; Vol. *1*.
(36) Umeda, T.; Kumaki, D.; Tokito, S. Surface-energy-dependent Field-effect Mobilities up to 1 cm2/V s for Polymer Thin-film Transistor. *J. Appl. Phys.* **2009**, *105*, 024516.
(37) Wang, C.-F.; Su, Y.-C.; Kuo, S.-W.; Huang, C.-F.; Sheen, Y.-C.; Chang, F.-C. Low-Surface-Free-Energy Materials Based on Polybenzoxazines. *Angew. Chem., Int. Ed.* **2006**, *45*, 2248−2251.
(38) Drelich, J.; Miller, J. D.; Good, R. J. The Effect of Drop (Bubble) Size on Advancing and Receding Contact Angles for Heterogeneous and Rough Solid Surfaces as Observed with Sessile-Drop and Captive-Bubble Techniques. *J. Colloid Interface Sci.* **1996**, *179*, 37−50.
(39) Kim, Y. S.; Lee, Y.; Lee, W.; Park, H.; Han, S.-H.; Lee, S.-H. Effects of Molecular Weight and Polydispersity of Poly (3-hexylthiophene) in Bulk Heterojunction Polymer Solar Cells. *Curr. Appl. Phys.* **2010**, *10*, 329−332.
(40) Gasperini, A.; Sivula, K. Effects of Molecular Weight on Microstructure and Carrier Transport in a Semicrystalline Poly(thieno)thiophene. *Macromolecules* **2013**, *46*, 9349−9358.

DOI: 10.1021/am505197b
ACS Appl. Mater. Interfaces 2015, 7, 1078−1086